Lifetime of a freely decaying hollow atom

M. Werl [1,*] T. Koller [1] P. Haidegger [1] S. Wrathall [1] L. Eßletzbichler [1] A. Niggas [1]
F. Aumayr [1] K. Tőkési [2] and R. A. Wilhelm [1,†]
[1]TU Wien, Institute of Applied Physics, 1040 Vienna, Austria
[2]HUN-REN Institute for Nuclear Research (ATOMKI), 4026 Debrecen, Hungary

(Received 18 July 2024; accepted 22 January 2025; published 18 February 2025)

Hollow atoms (HAs) are an exotic type of matter formed when a highly charged ion impacts on a surface, capturing multiple electrons into highly excited states, leaving intermediate electronic states empty. Although experimental fingerprints of HAs were found in high-resolution x-ray spectra, it has been widely believed that HAs decay too rapidly to be studied directly. Using a simulation code for the full deexcitation cascade of the HAs, based on rates from atomic structure codes for highly excited states, we show that the lifetime of an HA, scattered under very grazing angles from a surface, can reach several tens of ps in free decay. In additional experiments, we use Ar^{14+} ions on a Ni(110) surface under incidence angles below 0.5°. Comparing ion charge state distributions after scattering between experiment and simulation, we discuss the role of surface-stimulated decay in most interactions. We show that by minimizing the incidence angle, the influence of surface-near processes can be reduced and that HAs can exist for several picoseconds in free space.

DOI: 10.1103/PhysRevResearch.7.013176

I. INTRODUCTION

Atoms in highly excited states with multiple electronic core holes are fundamentally interesting building blocks to study QED effects [1,2] and to build optical clocks [3,4]. Rydberg atoms contain one or few electrons in excited states with high principal quantum numbers n [5]. Especially interesting are their significant dipole moments, stemming from their remarkable size: The radius scales with n^2 and in some cases, radii on the order of μm (for states with $n = 110$) were recorded [6]. Rydberg atoms can be produced by different means, e.g., laser excitation, which creates an energetically well-defined population. However, this method is limited mostly to alkali metals, as the valence electron binding energy of other elements is too high for fine-tunable optical frequency lasers [6]. By using a multi-stage process involving supersonic beams to preexcite atoms, optical excitation can still be utilized to create Rydberg states in noble gases [7]. Another means of production, common in astrophysical and laboratory plasmas, is electron impact excitation [8] or charge exchange ionization [9]. In both cases, the energy transfer is ambiguous, making it difficult to observe well-defined Rydberg states. While also doubly excited Rydberg atoms have been recorded [10], multiply excited states are usually limited to lower n states. Autoionization of doubly excited states typically limits their lifetime to some fs [11,12] and the state may therefore decay before any subsequent excitation is possible. Multiply excited states are usually only found in high-collisionality plasmas, where they can be used for plasma diagnostics [13]. High-intensity free electron laser (FEL) pulses can now be used to create multiply excited clusters [14–16], or to form double core holes by subsequent absorption of two x-ray photons in intense FEL pulses [17]. However, going from double to multiple core holes in a FEL might prove challenging because of the increasing demand for higher intensities to reach these interesting, yet exotic types of matter. Hollow atoms (HAs), first discovered by Briand *et al.* using high-resolution x-ray spectroscopy [18] may provide an alternative route. Essentially, HAs are multiply excited atoms, where several electrons occupy high-n states. They form upon slow (highly) charged ion impact on a conductive surface, where *slow* refers to ion impact velocities much smaller than the target materials Fermi velocity. Charge transfer of the weakly bound conduction-band electrons leads to resonant electron capture. For typical material work functions of ∼5 eV, electrons are captured into states with $n \sim q_{in}$, where q_{in} is the incoming charge state [19]. HAs formed in this way are typically referred to first-generation HA1s [20]. HAs can be created from basically any element, which is ionized and extracted from conventional ion sources (up to U^{92+} [21]) and the maximal n to be populated can be tuned with q_{in} and the target material work function. While there is experimental evidence for the formation of HAs [20,22–26], they are considered to exist only in front of a surface for the duration of the ion impact, which is on the order of a few femtoseconds.

Based on a HA cascade code with atomic decay rates obtained using the atomic code (FAC) [27], we predict that an HA can have a free decay lifetime of up to several 10 ps. This makes them available for (time-synchronized) spectroscopic

*Contact author: werl@iap.tuwien.ac.at
†Contact author: wilhelm@iap.tuwien.ac.at

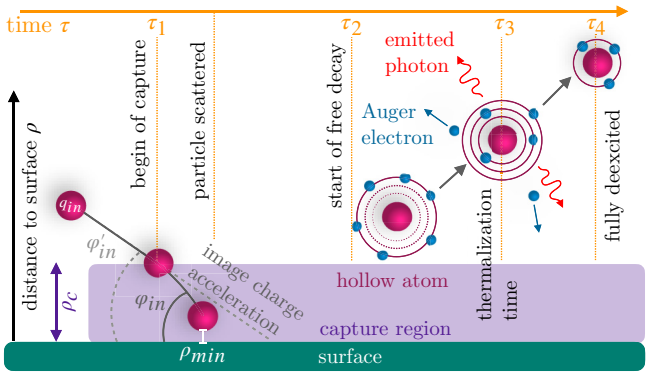

FIG. 1. Upon impact on a surface, an HCI (red) resonantly captures electrons (blue) into states with $n \sim q_{\mathrm{in}}$, forming an HA. Subsequently, it deexcites radiatively and nonradiatively, until all electrons reach a stable ground state.

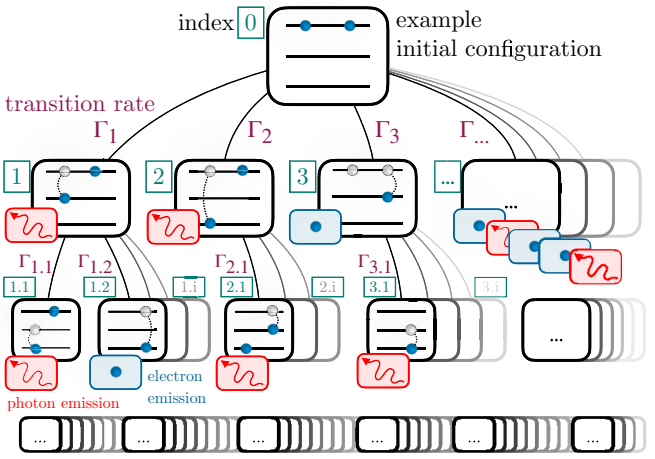

FIG. 2. For a given (excited) electron configuration, each deexcitation step contains many parallel branches. Every process is associated with a transition rate Γ and the ejection of secondary particles (photon or electron).

analysis. For instance, by using multiply excited Rydberg states as a perturbation while studying core-shell electronic dipole transition moments could provide stringent tests for fundamental QED studies [4]. To preserve the HA for this extended time period, any stimulated decay owing to the presence of the surface [28] must be avoided. In addition to our theoretical predictions, we show experimental data for a geometry, which avoids surface-near deexcitation as much as possible. We find indications for long-lived HAs and discuss differences to our theoretical predictions.

II. METHOD

A. Theoretical modeling

This paper extends a simulation code package originally designed to describe ion transmission through (micro)capillaries [29]. Projectiles with variable initial conditions, such as mass, energy, or charge state, are traced. Image charge effects and the particle trajectories are computed self-consistently and the formation of the HAs is described with the classical over-the-barrier (COB) model [19]. A Monte Carlo approach with coupled rate equations is then used to describe the deexcitation.

For the sake of clarity, we divide a particle trajectory into two regions, the capture and the free decay region, respectively, see Fig. 1. The capture region (shaded in purple) is characterized by a distance at which the electrostatic potential caused by the presence of the ion in front of the surface is equal to or smaller than the material work function W. Here, electrons are resonantly captured. The first capture occurs at a distance of $\rho_c = \frac{1}{2W}\sqrt{8q_{\mathrm{in}}+2}$ above the surface [19] (ρ_c and W are given in atomic units here), usually in the range of $8-30$ Å. An electron capture reduces the projectile charge state q and because of the corresponding modification of the image charge potential, the next capture happens at a smaller ρ. Inside the capture region resonant loss—the counterprocess to resonant capture—is also considered. As the projectile approaches, image charge acceleration becomes more significant, increasing the projectile incidence angle $\varphi_{\mathrm{in}} > \varphi'_{\mathrm{in}}$, where φ'_{in} would be the incidence angle neglecting image charge effects. After reaching a minimal distance ρ_{min}, the particle is scattered. The scattering kinematics are not explicitly modeled in this paper, but ρ_{min} is computed based on a set of equations described in [30], valid for atomically flat surfaces and small angles of incidence. In reality, atomic-scale flatness over a range of some 10–100 nm is sufficient to reproduce theoretical predictions.

Captured electrons begin to deexcite immediately via radiative and Auger-Meitner (AM) pathways. The loss of an electron inside the capture region is typically followed by the (re)capture of another electron from the surface. After scattering, once the distance is larger than ρ_c, no further capture is possible. This marks the free decay region, where the projectile decays exclusively via AM and radiative processes.

Especially in the case of high incident charge states, many electrons can be captured within the capture region. This marks the beginning of a deexcitation cascade as sketched in Fig. 2: From an initial state (index 0) with a corresponding electron configuration, many different pathways and transition processes lead toward a stable (ground) state. Each transition is associated with a rate Γ_{if} and the ejection of secondary particles; for a radiative transition a photon, and for AM, an Auger electron. To model this cascade, a Monte Carlo approach with coupled rate equations is used. Transition rates can go up to $10^{15}\,\mathrm{s}^{-1}$; therefore a time step of $dt = 10^{-16}\,\mathrm{s}$ was used for the simulations presented here to ensure a sufficient resolution of all relevant processes.

Important for this study is the use of transition rates for highly excited states with many (spectator) electrons in various intermediate shells. For the multitude of different processes, especially for high n, this goes significantly beyond previous studies [19,29], which considered mostly initial charge states <10 for light ions. The availability of slow, heavy, highly charged ions up to U^{92+} at keV energies [31] therefore demands a new approach. We use rates extracted from literature [32] and complement them with calculated rates from the FAC atomic structure code package [27]. It should be noted that great progress was recently achieved in understanding particularly long-lived transitions in highly charged ions [33,34], but the decay of an HA is determined mostly by the fastest possible transitions as they imply the

largest branching ratio in all possible processes. Different atomic structure codes, such as the Cowan code [35,36] and the JAC code package [37] were compared and show good agreement (see Fig. 7 in the Appendix).

Since the initial population of the HA is essential and follows from the COB model, which only depends on n and no other quantum numbers, we reduced the problem of the cascade to include only the quantum numbers n of involved electrons. We used the single-configurational average (SCA), also used in previous paper [36]. Here, the averaged rate is given by $\Gamma_{\mathrm{SCA}} = \frac{\sum_i w_i \sum_f \Gamma_{if}}{\sum_i w_i}$, where $w_i = (2j_i + 1)$ is a statistical weight depending on the initial state's total angular momentum j_i and Γ_{if} is the transition rate from state i to f. Selection rules for the angular momentum quantum number j disproportionately affect and, in practice, lower the resulting SCA-rates significantly. Our objective was to get lower bounds for the lifetimes, and therefore only the fastest type of transitions for j was considered. This means $n_i p \rightarrow n_f s$-type transitions in the radiative case and $n_i s \rightarrow n_f s$ transitions in the AM case, where n_i/n_f are the initial/final n and p/s are the respective l quantum numbers (1 and 0). Despite being particularly short lived, Coster-Kronig transitions [38] were not included, as they require very specific electronic configurations that appear only in a negligible amount of cases in the ensemble of all calculated trajectories.

The SCA-based rates for both types of transitions were fit with nonlinear functions [see Eqs. (1) and (2) in the Appendix], also taking screening by spectator electrons into account. The obtained fit function for radiative transitions depends on n_i and n_f, and the well-established scaling of radiative rates with the nuclear charge of Z^4 [39]. The rate for AM transitions uses n_i and n_f of the respective electron and the shell of the ejected Auger electron n'. The fit functions use data for H-like transitions for the radiative case and He-like transitions for the AM case. The effect of additional spectator electrons, which do not directly participate in the process but influence the process rate, was included by using multiplicative factors Ω: They depend on the number of spectator electrons and the n of the states they occupy. Details on all the fit functions can be found in the Appendix and Fig. 8 therein.

For both types of transitions, the corresponding rates tend to decrease towards higher n_i, implying that high-n shells can be populated relatively long. This is consistent with experimental observations for high-n Rydberg states [40]. AM transitions show a clear preference towards small $\Delta n = n_f - n_i$ and their rates decrease rapidly for $\Delta n > 1$. In the radiative case, the opposite is true: Transitions with higher Δn are generally faster.

The lifetime for each individual pathway in the cascade can be largely different and it is not straightforward to define (average) lifetimes for HAs. Therefore, this study uses a few distinct time points of a projectiles trajectory. These are (see also Fig. 1):

(i) τ_1: Projectile enters the capture region, electrons can be captured ($\rho = \rho_c$).

(ii) τ_2: Particle exits the capture region ($\rho \geqslant \rho_c$). No further capture is possible and the projectile starts to decay freely, i.e., without influence of the surface.

(iii) τ_3: The projectile has "thermalized", i.e., the number of electrons in excited states $N(\tau_3)$ has dropped to $\frac{1}{e} \times N(\tau_2)$ of the value at τ_2.

(iv) τ_4: No more electrons are in excited states, particle has fully deexcited.

We use two different ways to define the lifetime of an HA, since the number of electrons in excited states decays exponentially. The first is the thermalization time in the free decay region, i.e., the time difference $\tau_3 - \tau_2$. For the second, we use the full lifetime of an HA, i.e., the time difference from the first captured electron (τ_1) until all electrons have decayed to their ground state (τ_4).

Simulations presented in this paper were all performed for noble gases (He, Ar, Kr, Xe) of varying charge states scattering on an HOPG surface. To compare HAs formed by different ion species and, hence, different scattering kinematics, incident energies and angles were chosen such that the ratio of critical capture radius ρ_c and distance of minimal approach $\rho_{\mathrm{min}}(E, \varphi_{\mathrm{in}})$ remains roughly constant $\frac{\rho_c}{\rho_{\mathrm{min}}} \approx 7$. This limits the interaction time with the surface to between 0.15 ps for Ne and 0.35 ps for Xe, being comparable over all charge states within a projectile species. Specifically, we varied the ion kinetic energies from $\sim$1 keV at $q_{in} = 5$ to $\sim$300 keV at $q_{in} = 50$ and φ_{in} between 0.05° and 1°.

B. Experimental setup

Experiments were also performed using the ion beam spectrometer at TU Wien [41]. The experiments were done with Ar^{14+} ions at kinetic energies of 63 keV under very grazing angles of incidence on a well-prepared Ni(110) single crystal. The sample was prepared using repeated cycles of sputter cleaning with 0.5 μA of Ar^+ ions at energies of 1.5 keV for about 30 minutes and subsequent rapid thermal annealing at 500°C. The surface quality was then verified using low-energy electron diffraction (LEED). The experiments were performed at a base chamber pressure of 2×10^{-9} mbar. The scattered particles were detected using a 2D position-sensitive microchannel plate (MCP) detector. After the interaction, the scattered particles first pass through a slit and then through a pair of deflection plates to differentiate outgoing charge states. To achieve very grazing angles, we first confirmed that the sample had a nanoscale flat surface (over an area of several 100 nm) as measured using an atomic force microscope under ambient conditions prior to sample preparation in the ion beam spectrometer. Then, the sample and the ion beam were aligned with respect to the vacuum chamber using a laser diode in conjunction with the MCP. As a final step, the sample was rotated in steps of 0.1° until scattered particles were detected on the MCP. The resulting scattering angle distribution was used as a control parameter for the incident angle. Uncertainty in the scattering angle is primarily determined by the sample manipulator uncertainty, specified as ±0.1°. The MCP image of the beam (without any sample) lets us directly measure the beam divergence in our experiment, which is below 0.1°.

III. RESULTS

Figure 3 shows the lifetime distributions for some select cases. The orange histograms show the thermalization

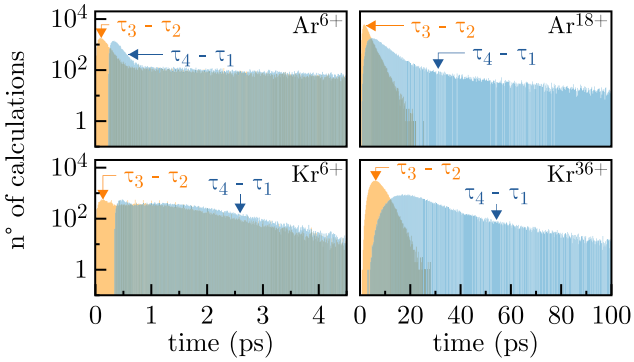

FIG. 3. Lifetime distributions for selected simulations. The orange histograms represent the thermalization time ($\tau_3 - \tau_2$), the blue ones the full lifetime ($\tau_4 - \tau_1$). A total of 10^5 particles were simulated per ion charge state.

times while the blue histograms show the full lifetimes (cf. Sec. II A). For low initial charge states, such as Ar^{6+} and Kr^{6+}, the two distributions appear similar, with the full lifetimes shifted slightly towards higher values. For higher charge states, e.g., Ar^{18+} and Kr^{36+}, the difference in the distributions for the two definitions is more evident.

The median values of the lifetime distributions (cf. Fig. 3) were used to define the mean lifetime for a specific charge state. Figure 4 shows these lifetimes as a function of the projectile type and charge state. The upper panel shows the full lifetime ($\tau_4 - \tau_1$) and the lower panel shows the thermalization time ($\tau_3 - \tau_2$). While the data for Ne, Ar, and Kr go up to bare projectiles, Xe only has data up to Xe^{49+} owing to numerical instabilities for higher charge states.

To benchmark the outcome of our calculations to experiments one can use the final charge state distribution at τ_4. The final charge state distributions for three different initial charge states Ar^{6+} (blue), Ar^{12+} (red), and Ar^{18+} (green), are shown in Fig. 5(a). During the deexcitation cascade, AM processes cause a projectile to recharge and especially in the free decay

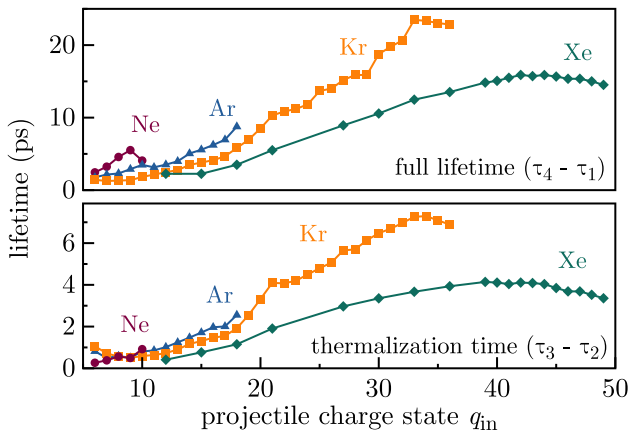

FIG. 4. Calculated lifetimes of hollow atoms formed by grazing scattering of highly charged ions on HOPG as a function of their initial charge state. Red circles represents Ne, blue triangles Ar, orange squares Kr, and green diamonds Xe. The upper panel shows the full time and the lower panel shows the thermalization time.

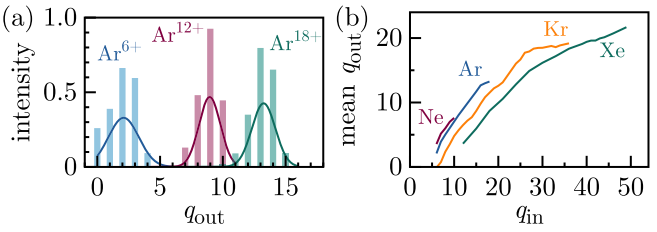

FIG. 5. (a) Final charge state distributions for incoming charge states of Ar^{6+} (blue), Ar^{12+} (red), and Ar^{18+} (green). (b) Mean of the final charge state distribution as a function of the initial charge state for Ne (red), Ar (blue), Kr (orange), and Xe (green).

region, where no further electrons can be (re)supplied, the HA can recharge almost back to q_{in}. From the distributions in Fig. 5(a), we analyzed the mean values of the final charge state distributions and they are shown in Fig. 5(b) as a function of q_{in} and projectile type.

In general, we find that the lifetimes of HAs formed by grazing-incidence scattering are in the range of several picoseconds (cf Fig. 4). This is potentially long enough to perform optical spectroscopy during the deexcitation with modern ultrafast laser systems of various wavelength regions including even X-FEL-based systems. The full lifetime is longer than the thermalization time by a factor of about three, consistent over all projectiles and charge states. The time spent inside the capture region, $\tau_2 - \tau_1$, is very short (0.15–0.35 ps) and contributes very little to the lifetime, especially at higher q_{in}. The difference in the two lifetime definitions can therefore be attributed mostly to some electrons, which might remain in long-lived high-n states, especially if energetically no more AM processes are possible. The character of a multiple excited state will most likely be gone then, implying that the time where one can study the decay sequence is probably limited to the thermalization time.

For the same q_{in}, lighter projectiles tend to have longer lifetimes. This can be attributed to the scaling of radiative decay rates with Z^4, leading to faster deexcitation and correspondingly shorter lifetimes for heavier projectiles. Generally, higher q_{in} have longer lifetimes. However, if the projectile has initial core shell holes, the lifetime can actually decrease. This is especially noticeable for Ne^{10+} (two K-shell holes), Kr^{27+} (one L-shell hole), and Kr^{35+}-Kr^{36+} (one or two K-shell holes, respectively). Rates increase towards smaller n_f, and K-shell holes get filled substantially faster than empty states in $n > 1$. While this applies to both radiative and AM transitions, AM transitions decrease rapidly with larger Δn, meaning that core shell holes are preferentially filled by radiative transitions.

For lower initial charge states, such as Ar^{6+}, there are still some neutral final charge states [see Fig. 5(a)]. For higher charge states (Ar^{12+}, Ar^{18+}) the distribution shifts to higher final charge states and there are no neutral or low final charge states. Heavier elements tend to have a lower final charge state for the same q_{in}. This can again be attributed to the higher radiative rates for heavier elements: More electrons decay radiatively rather than by AM transitions, leading to less recharging.

Let us now compare our results with experimental results. Figure 6(a) shows Ar^{14+} ions with kinetic energies of 51 keV

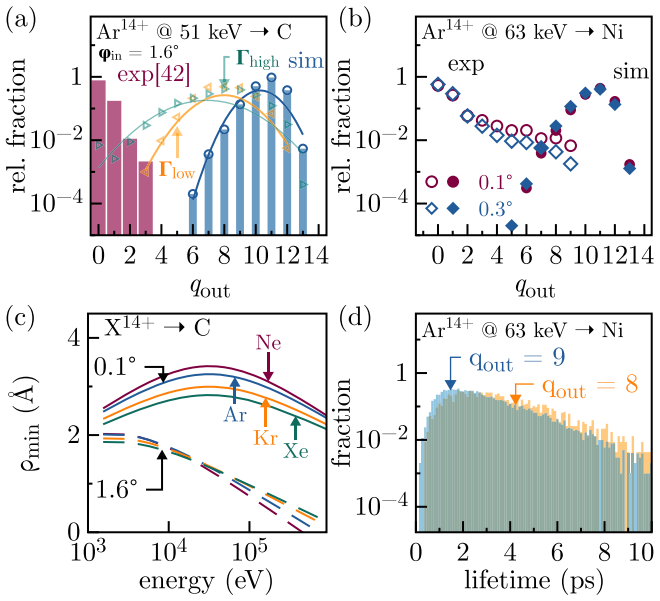

FIG. 6. (a) Charge state distribution of Ar^{14+} at 51 keV onto a C surface with $\varphi_{in} = 1.6°$. Red shows experimental results [42], while blue shows simulated results. The green/orange curves show the simulation results when the magnitude of the deexcitation rates is higher/lower by an order of magnitude. (b) Charge state distribution of Ar^{14+} at 63 keV onto a Ni(110) surface. Open symbols show experiments performed at TU Wien, while full circles depict results from our simulations. Red/blue show incoming angles of $\varphi_{in} = 0.1°/0.3°$, respectively. (c) Distance of minimal approach ρ_{min} as a function of energy and incoming angles φ_{in} for different projectiles with $q_{in} = 14$ for impact on a C surface. (d) Lifetime distribution for trajectories from Fig. 6(b) with final charge states of $q_{out} = 8$ (orange) and $q_{out} = 9$ (blue) for the case of $\varphi_{in} = 0.1°$.

scattered on an HOPG surface with an incident angle of 1.6° [42]. The experiment (red) found almost all particles to be neutral after the interaction, with only small fractions of Ar^{1+}, Ar^{2+}, and Ar^{3+} detected after the interaction. Simulations (blue) without surface-near processes predict a charge state distribution centered around Ar^{11+}/Ar^{12+}, with the lowest charge state being Ar^{9+}. The interaction time in this simulation was on the order of 10–100 fs, comparable to our τ_2 time. In Fig. 6(b), experimental and simulation results of scattering Ar^{14+} at energies of 63 keV from a Ni(110) single crystal are shown. Red/blue depict incoming angles of $\varphi_{in} = 0.1°/0.3°$. The open symbols show measured charge state fractions, while full symbols show results from our simulations. While in this experiment the largest fraction of particles was neutral, high final charge states up to Ar^{9+} were also observed; their relative fraction decreased in the case of $\varphi_{in} = 0.3°$ with respect to $\varphi_{in} = 0.1°$. The simulations predict a distribution centered around higher charge states, with no neutral or low final charges.

To get an estimate of the uncertainty of our rate-based Monte Carlo approach, the magnitude of the (final) rates was varied. Orange/green symbols in Fig. 6(a) show the resulting final charge state distribution when decreasing/increasing the process rates by an order of magnitude. The solid lines help guide the eye on how the resulting distributions shift. Both ten-times higher or lower rates shift the distribution towards lower average final charge states, but for different reasons. In the case of lower rates (orange), there is a higher proportion of (nonrecharging) radiative deexcitations, leading to a lower (and broader) final charge state distribution. In the case of higher rates (green), the rates are so fast that most of the deexcitation has already taken place while the projectile is still inside the capture region where electrons can be resupplied. As a result, some particles are already fully or mostly neutralized at the start of the free decay region and cannot recharge as much.

IV. DISCUSSION

In past experiments, the final charge states of highly charged ions after interactions with materials have been measured in both in grazing-incidence scattering [42–44] as well as transmission through 2D materials [45–47]. In contrast to the simulation results presented in this paper, the measured final charge states were mostly neutral, implying the presence of deexcitation mechanisms other than those considered here. In the case of transmission through 2D materials, such as a single layer of graphene, the interaction time was very short (1 fs) [45]. Still, this interaction time was enough for the projectile to almost fully neutralize. In fact, the time dependence of the charge decay was measured in the experiment and showed an exponential decay with a time constant of $\sim 2 - 10$ fs [47].

Figure 6(a) shows that most particles in the experiments are neutral after the interaction under very grazing scattering from atomically flat surfaces. Because of the (single-configurational) averaged rates in our model, we might be underestimating the impact of particularly long-lived states and forbidden types of transitions. However, especially in the case of higher initial projectile charge states (and consequently more captured electrons), there are typically many pathways through which the electrons can deexcite. We estimate the effect of forbidden transitions on both the lifetime and final charge state distributions to be negligible for a large ensemble of particles. This, in turn, also means that our model is less accurate for lower initial projectile charge states.

The remaining discrepancy between simulation and experiment could be explained by additional, different deexcitation mechanisms upon ion impact on a surface. Interatomic Coulombic decay (ICD) was proposed [28] to be the most likely candidate to explain these observations, as it does not recharge the projectile and is the only mechanism that is sufficiently fast (fs). This process is known to be extremely dependent on the distance between projectile and target [47,48] and drops rapidly for distances larger than ~3 Å. Recently, it was shown that the expected electron emission from ICD indeed depends on the interatomic separation HCIs transmitting through graphene [49]. Figure 6(c) shows the distances of closest approach ρ_{min}, computed using the approach presented in [30], as a function of projectile energy for two different angles of incidence and particles with $q_{in} = 14$. In general,

lower energies tend to increase $\rho_{\min}$. For very low energies, the image charge becomes more dominant and $\rho_{\min}$ decreases again. In previous transmission and grazing-incidence experiments [42–44], the minimal distance between projectile and target was always $\lesssim 3$ Å. To achieve $\rho_{\min} \gtrsim 3$ Å, a scattering geometry with very grazing angles of incidence can be used. This decreases the effect of ICD and one would expect a tendency toward higher exit charge states. This is clearly visible when comparing the results from Figs. 6(a) and 6(b). As φ_{in} gets smaller, a higher proportion of high final charge states is measured, implying that the effect of ICD can be (at least to an extent) limited. While both experiments used slightly different energies and targets, the targets have similar work functions of $W = 4.6$ eV [50] for HOPG and 5.04 eV [51] for Ni(110) and therefore we believe the influence to be minor. The energies of the ions were very comparable for the two experiments in Figs. 6(a) and 6(b). The lifetime distribution of the trajectories with $q_{\text{out}} = 8$ (orange) and 9 (blue) for the case with $\varphi_{\text{in}} = 0.1^\circ$ is shown in Fig. 6(d). The lifetimes of several picoseconds compare well to the overall predicted result from Fig. 4. This implies the possibility of actually preparing hollow atoms with lifetimes of picoseconds in experiments capable of producing ions in high enough initial charge states [41,52–55].

An alternative approach to scattering could be the use of thin, perforated membranes. Here, ions can pass through pinholes and capture electrons from the material at consistently large interatomic distances, minimizing ICD effects. Ideally, the membranes should be as thin as possible. We recommend thicknesses on the order of a few nm. The ideal pore radius would be on the order of the capture radius (8–30 Å, see Sec. II A) to ensure trajectories passing far enough from the surface while still capturing electrons. The existence of HAs could be measured *in situ* using photoelectron spectroscopy [56] and by measuring the deexcitation spectra [25,26]. The charge state after the interaction helps in understanding the branching ratio of AM processes during the deexcitation process.

Considerable efforts have been made to find accurate and suitable theoretical descriptions of ICD processes [47,57]. These approaches treated the captured electrons either in an excited or a stabilized/ground state, without explicitly calculating the dynamics. These approaches worked well to describe past ion transmission experiments, where deexcitation via radiative and Auger pathways was assumed to play a negligible role. To describe the processes occurring during grazing-scattering geometries, and consequently at larger distances from the surface, these models need to be adapted.

V. CONCLUSIONS

We presented a simulation approach that describes how highly excited ions form a hollow atom (HA) through electron capture from a surface and how it subsequently deexcites through typical radiative and Auger-Meitner (AM) pathways. This way we were able to estimate the lifetimes of HAs as well as their final, steady-state charge state distribution when decaying in a vacuum. We showed that the lifetimes of these HAs, in our case formed by grazing-incidence scattering from a surface, can reach up to 10 ps—significantly longer than previously anticipated—making the HAs long-lived enough to be studied in currently developed experiments with similar timing resolution [58]. By comparing our simulation results to both past and current experiments, we showed that charge exchange with the surface is significantly more effective for larger incoming angles, leading to more neutral final charge states that cannot be explained using radiative and AM processes alone. We discussed the importance of accounting for other deexcitation processes, such as ICD, to describe highly charged ion neutralization. We outlined other strategies to avoid surface-near quenching of HAs.

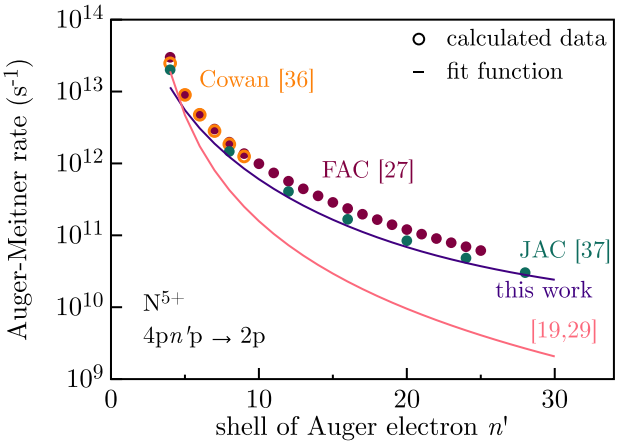

FIG. 7. Comparison of Auger-Meitner transition rates for transitions of type $4pn'p \rightarrow 2p$ in a N^{5+} ion as a function of the shell of the Auger electron n'. To consider the fine structure, the single configuration average (see text) was used. The dots are rates computed with different atomic structure codes, the lower line is for Refs. [19,29], and the solid line for this work representing the fit according to Eq. (1).

ACKNOWLEDGEMENT

We thank S. Fritzsche for help with the JAC code package and M. F. Gu for support with the FAC code as well as R. Lucrezi for help with nonlinear fitting. Financial support by the Austrian Science Fund (FWF Grant DOIs 10.55776/I4914, 10.55776/P36264, 10.55776/Y1174) is gratefully acknowledged.

APPENDIX

Figure 7 shows single-configuration average (SCA, see main text) Auger-Meitner rates for the transition $4pn'p \rightarrow 2p$ as a function of the shell of the Auger electron n'. The orange points are literature data [36] and were calculated using the Cowan code [35], the green points were computed using the JAC [37] and the red data points were computed using the FAC code package [27]. The pink fit function was commonly used in previous studies [19,29], while the purple function was obtained and used throughout this paper.

The function for the rates of Auger-Meitner processes used in this paper is

$$\Gamma_{\mathrm{AM}}(n_i, \Delta n = (n_f - n_i), n') = \exp\left(\alpha_1 \log(n_i + \alpha_2 \Delta n + \alpha_3) e^{\alpha_4 \Delta n + \alpha_5 n_i} + \alpha_6 e^{-\alpha_7 \Delta n - \alpha_8 n_i} + \alpha_9 \frac{\log(n_i)}{\Delta n} + \alpha_{10} \Delta n + \alpha_{11} e^{\alpha_{12} n'} + \frac{\alpha_{13}}{n'} + \alpha_{14}\right) \quad (1)$$

and depends on the initial/final shell n_i/n_f of the respective electron and the shell of the Auger electron n'. Note that for the release of an Auger electron, the energy released during the transition ΔE has to be larger than the binding energy of the released electron $\Delta E > E_B(n')$, restricting the possible values for n'. Since AM processes are essentially electron-electron scattering processes, Z was found to have a very negligible effect on AM transition rates.

The fit function for the rates of radiative transitions depends on n_i, n_f and the nuclear charge Z,

$$\Gamma_{\mathrm{rad}}(Z, n_i, n_f) = Z^4 \exp(\beta_1 e^{\beta_2 (n_i - n_f)} e^{\beta_3 n_i} + \beta_4 e^{\beta_5 n_i} e^{\beta_6 n_f} + \beta_7 e^{\beta_8 n_i} + \beta_9). \quad (2)$$

The coefficients in the fit functions are given by

α_1	α_2	α_3	α_4	α_5	α_6	α_7
2.006	–1.026	0.728	0.011	–0.040	4.493	0.368
α_8	α_9	α_{10}	α_{11}	α_{12}	α_{13}	α_{14}
–0.003	0.215	–0.184	7.206	–0.067	7.475	18.739

and

β_1	β_2	β_3	β_4	β_5
2.803	0.741	–0.689	15.230	–0.063
β_6	β_7	β_8	β_9	
–0.090	12.707	–1.323	5.590	

Figure 8(a) shows Auger-Meitner rates for the transition n_ip n'p $\rightarrow n_f$ p as a function of n_i. The contours are for different values of $\Delta n = n_f - n_i$ and for every transition the lowest energetically possible value for n' was taken. The open circles are rates computed using the FAC and the solid lines represent the fitted function. Figure 8(b) shows the same but for radiative rates. Here, rates for nitrogen ($Z = 7$) are shown, as experimental data was also available in this case [32].

The effect of electrons not directly involved in a process, namely spectator electrons, was accounted for by using extra factors Ω_{AM} in the case of AM transitions and for radiative cases Ω_{n_i}. In the case of Auger-Meitner transitions, the adapted rate then becomes

$$\Gamma'_{\mathrm{AM}} = \Gamma_{\mathrm{AM}} \cdot \Omega_{\mathrm{AM}}(N, Z).$$

The factor Ω_{AM} depends on the number of electrons N in shells $n_f < n < n_i$ and on the nuclear charge Z,

$$\Omega_{\mathrm{AM}} = 1 - \left(\frac{\gamma_1}{Z + \gamma_2} - \gamma_3\right) N \exp(-(\gamma_4 - \gamma_5 Z) N).$$

Electrons in other shells have a negligible effect. The coefficients are given by

γ_1	γ_2	γ_3	γ_4	γ_5
4.0053	8.7455	0.0297	0.0569	0.0009

For the radiative transition, the nuclear charge becomes $Z \rightarrow Z\Omega_{n_i}$ and correspondingly, the rate becomes

$$\Gamma'_{\mathrm{rad}} = \Gamma_{\mathrm{rad}} \cdot \Omega^4_{n_i - 1},$$

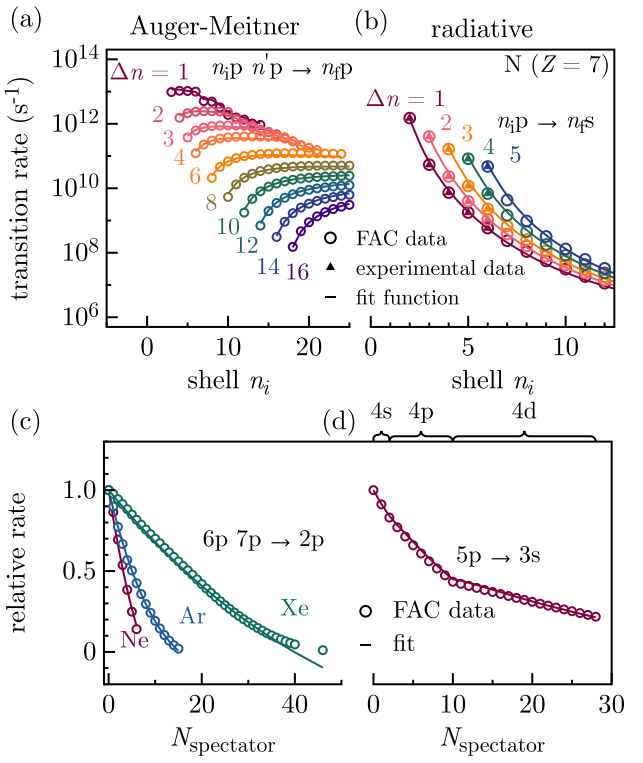

FIG. 8. Fit functions for the transition rates used in this paper. The circles are data computed using FAC, while the solid lines are the fit functions obtained from the calculated data. Panel (a) shows Auger-Meitner rates as a function of n_i with $\Delta n = n_f - n_i$ as contours, with n' taking on the lowest energetically possible shell. Panel (b) shows the same for the radiative rates for nitrogen. Experimentally available data are also included (as triangles) where available. Panel (c) shows the relative rates $\frac{\Omega(N)}{\Omega(N=0)}$ obtained by using the screening factor Ω for the Auger-Meitner rates as a function of the number of spectator electrons N for Ne (red), Ar (blue), and Xe (green). The figure shows the transitions of type $6p\ 7p \rightarrow 2p$ and spectator electrons were populated in shells with $2 < n < 6$. Panel (d) shows the relative rate for radiative rates, in this case for the transition $5p \rightarrow 3s$, while filling electrons in the $n = 4$ shell. The effect of filling different subshells (labeled at the top) is accounted for.

where the factor Ω is obtained iteratively

$$\Omega_n = \Omega_{n-1}\left(\frac{Z\Omega_{n-1} - N}{Z\Omega_{n-1}}\right)^{\alpha(n_i,n_f,n)}$$

and $\Omega_0 = 1$. The exponent $\alpha(n_i, n_f, n)$ is given by

$$\alpha(n_i, n_f, n) = \begin{cases} 1.23 - 0.8\frac{n-1}{n_f} & \text{for } n < n_f \\ 0.65 - 0.6\frac{n_f-2}{n_f} & \text{for } n = n_f \\ 0.47 - 0.29\frac{n-n_f}{n_i-n_f} & \text{for } n_f < n < n_i. \end{cases}$$

Finally, if there is at least one electron in n_f, the (total) rate is additionally multiplied by 0.52,

$$\Gamma'_{\text{rad}} = \Gamma_{\text{rad}} \cdot \Omega^4_{n_i-1}(1 - 0.48\text{H}(N_{n_f} - 1)),$$

where $\text{H}(x)$ is the Heaviside step function.

Figure 8(c) shows the relative rates $\frac{\Gamma(N)}{\Gamma(N=0)}$ for AM transitions as a function of the number of spectator electrons N. The figure shows the transitions of type $6p\ 7p \rightarrow 2p$ with electrons filled in shells in between for Ne (red), Argon (blue), and Xe (green). For Xe, the fit deteriorates for $N > 40$ (and can become negative); however, it is practically never the case to find more than ≈20 electrons in shells $n_f < n < n_i$ and, therefore, the quality of the fit was deemed acceptable. Panel (d) shows the relative radiative rates $\frac{\Gamma(N)}{\Gamma(N=0)}$ for transitions of type $5p \rightarrow 3p$, where electrons have been populated in the $n = 4$ shell. It can be seen that the fit also accounts for the change in rates following the filling of subshells, marked above the figure.

[1] J. Volz, R. Gehr, G. Dubois, J. Estève, and J. Reichel, Measurement of the internal state of a single atom without energy exchange, Nature (London) **475**, 210 (2011).

[2] J. Morgner, B. Tu, C. M. König, T. Sailer, F. Heiße, H. Bekker, B. Sikora, C. Lyu, V. A. Yerokhin, Z. Harman *et al.*, Stringent test of QED with hydrogen-like tin, Nature (London) **622**, 53 (2023).

[3] M. Berholts, R. Knut, R. Stefanuik, H. Wikmark, S. Saha, and J. Söderström, Quantum watch and its intrinsic proof of accuracy, Phys. Rev. Res. **4**, 043041 (2022).

[4] S. A. King, L. J. Spieß, P. Micke, A. Wilzewski, T. Leopold, E. Benkler, R. Lange, N. Huntemann, A. Surzhykov, V. A. Yerokhin *et al.*, An optical atomic clock based on a highly charged ion, Nature (London) **611**, 43 (2022).

[5] T. F. Gallagher, *Rydberg Atoms*, edited by A. Dalgarno, P. Knight, F. Read, and R. Zarc (Cambridge University Press, Cambridge, 2005).

[6] N. Sibalic and C. S. Adamas, *Rydberg Physics* (IOP Publishing, Bristol, 2018).

[7] T. Thiele, S. Filipp, J. A. Agner, H. Schmutz, J. Deiglmayr, M. Stammeier, P. Allmendinger, F. Merkt, and A. Wallraff, Manipulating Rydberg atoms close to surfaces at cryogenic temperatures, Phys. Rev. A **90**, 013414 (2014).

[8] J. A. Schiavone, D. E. Donohue, D. R. Herrick, and R. S. Freund, Electron-impact excitation of helium: Cross sections, n, and l distributions of high Rydberg states, Phys. Rev. A **16**, 48 (1977).

[9] F. J. Deck, E. A. Hessels, and S. R. Lundeen, Population of high-L sulfur Rydberg levels by ion–Rydberg-atom charge exchange, Phys. Rev. A **48**, 4400 (1993).

[10] W. E. Cooke, T. F. Gallagher, S. A. Edelstein, and R. M. Hill, Doubly excited autoionizing Rydberg states of Sr, Phys. Rev. Lett. **40**, 178 (1978).

[11] G. Jabbari, K. Gokhberg, and L. S. Cederbaum, Competition between interatomic Coulombic decay and autoionization of doubly-excited atoms, Chem. Phys. Lett. **754**, 137571 (2020).

[12] P. Zhang, J. Trester, K. Ueda, M. Han, T. Balčiūnas, and H. J. Wörner, Time-resolved multielectron coincidence spectroscopy of double Auger-Meitner decay following Xe $4d$ ionization, Phys. Rev. Lett. **132**, 083201 (2024).

[13] E. Träbert, The allure of high total angular momentum levels in multiply-excited ions, Atoms **7**, 103 (2019).

[14] L. S. Cederbaum, J. Zobeley, and F. Tarantelli, Giant intermolecular decay and fragmentation of clusters, Phys. Rev. Lett. **79**, 4778 (1997).

[15] A. C. LaForge, M. Drabbels, N. B. Brauer, M. Coreno, M. Devetta, M. Di Fraia, P. Finetti, C. Grazioli, R. Katzy, V. Lyamayev *et al.*, Collective autoionization in multiply-excited systems: A novel ionization process observed in helium nanodroplets, Sci. Rep. **4**, 3621 (2014).

[16] D. Iablonskyi, K. Nagaya, H. Fukuzawa, K. Motomura, Y. Kumagai, S. Mondal, T. Tachibana, T. Takanashi, T. Nishiyama, K. Matsunami, P. Johnsson, P. Piseri, G. Sansone, A. Dubrouil, M. Reduzzi, P. Carpeggiani, C. Vozzi, M. Devetta, M. Negro, F. Calegari *et al.*, Slow interatomic Coulombic decay of multiply excited neon clusters, Phys. Rev. Lett. **117**, 276806 (2016).

[17] I. Ismail, A. Ferté, F. Penent, R. Guillemin, D. Peng, T. Marchenko, O. Travnikova, L. Inhester, R. Taïeb, A. Verma, N. Velasquez, E. Kukk, F. Trinter, D. Koulentianos, T. Mazza, T. M. Baumann, D. E. Rivas, Y. Ovcharenko, R. Boll, S. Dold *et al.*, Alternative pathway to double-core-hole states, Phys. Rev. Lett. **131**, 253201 (2023).

[18] J. P. Briand, L. De Billy, P. Charles, S. Essabaa, P. Briand, R. Geller, J. P. Desclaux, S. Bliman, and C. Ristori, Subfemtosecond study of the hypersatellite-satellite cascade in "hollow" atoms, Phys. Rev. A **43**, 565 (1991).

[19] J. Burgdörfer, P. Lerner, and F. W. Meyer, Above-surface neutralization of highly charged ions: The classical over-the-barrier model, Phys. Rev. A **44**, 5674 (1991).

[20] H. Winter and F. Aumayr, Hollow atoms, J. Phys. B: At., Mol. Opt. Phys. **32**, R39 (1999).

[21] R. E. Marrs, S. R. Elliott, and D. A. Knapp, Production and trapping of hydrogenlike and bare uranium ions in an electron beam ion trap, Phys. Rev. Lett. **72**, 4082 (1994).

[22] J.-P. Briand, V. Le Roux, N. Béchu, S. Dreuil, G. Machicoane, M. Prior, and Z. Xie, The hollow atoms, Nucl. Instrum. Methods Phys. Res., Sect. B **154**, 166 (1999).

[23] W. Brandt, R. Laubert, M. Mourino, and A. Schwarzschild, Dynamic screening of projectile charges in solids measured by target x-ray emission, Phys. Rev. Lett. **30**, 358 (1973).

[24] J. Schwestka, R. Wilhelm, E. Gruber, R. Heller, R. Kozubek, M. Schleberger, S. Facsko, and F. Aumayr, The role of radiative de-excitation in the neutralization process of highly charged ions interacting with a single layer of graphene, Nucl. Instrum. Methods Phys. Res., Sect. B **422**, 63 (2018).

[25] P. Dergham, F. Aumayr, E. Lamour, S. Macé, C. Prigent, S. Steydli, D. Vernhet, M. Werl, R. A. Wilhelm, and M. Trassinelli, Toward probing surface magnetism with highly charged ions, Atoms **10**, 151 (2022).

[26] L. Jabłoński, D. Banaś, P. Jagodziński, A. Kubala-Kukuś, D. Sobota, I. Stabrawa, K. Szary, and M. Pajek, Experimental investigations of two-electron relaxation processes in Rydberg hollow atoms, X-Ray Spectrom. **52**, 430 (2023).

[27] M. F. Gu, The flexible atomic code, Can. J. Phys. **86**, 675 (2008).

[28] R. A. Wilhelm, E. Gruber, J. Schwestka, R. Kozubek, T. I. Madeira, J. P. Marques, J. Kobus, A. V. Krasheninnikov, M. Schleberger, and F. Aumayr, Interatomic Coulombic decay: the mechanism for rapid deexcitation of hollow atoms, Phys. Rev. Lett. **119**, 103401 (2017).

[29] K. Tőkési, L. Wirtz, C. Lemell, and J. Burgdörfer, Hollow-ion formation in microcapillaries, Phys. Rev. A **64**, 042902 (2001).

[30] H. Winter, Collisions of atoms and ions with surfaces under grazing incidence, Phys. Rep. **367**, 387 (2002).

[31] H.-J. Kluge, T. Beier, K. Blaum, L. Dahl, S. Eliseev, F. Herfurth, B. Hofmann, O. Kester, S. Koszudowski, C. Kozhuharov *et al.*, Chapter 7 HITRAP: A facility at GSI for highly charged ions, Adv. Quantum Chem. **53**, 83 (2008).

[32] A. Kramida, Yu. Ralchenko, J. Reader, and NIST ASD Team, NIST Atomic Spectra Database (ver. 5.11), [Online]. Available: `https://physics.nist.gov/asd⟨0:monospace ⟩⟨/0:monospace⟩` [2016, January 31]. National Institute of Standards and Technology, Gaithersburg, MD. (2021).

[33] N.-H. Rehbehn, M. K. Rosner, J. C. Berengut, P. O. Schmidt, T. Pfeifer, M. F. Gu, and J. R. C. López-Urrutia, Narrow and ultranarrow transitions in highly charged Xe ions as probes of fifth forces, Phys. Rev. Lett. **131**, 161803 (2023).

[34] Y.-M. Yu and B. K. Sahoo, Energy-level-crossing study of forbidden transitions in highly charged ions with $(n = 4, 5)$ d^6 and $(n = 4, 5)$ d^8 configurations for making optical clocks, Phys. Rev. A **109**, 023106 (2024).

[35] R. D. Cowan, *The Theory of Atomic Structure and Spectra*, Los Alamos Series in Basic and Applied Sciences (University of California Press, Berkeley, 1981).

[36] P. Palmeri, P. Quinet, N. Zitane, and N. Vaeck, Calculation of Auger rates for complex hollow-atom configurations, J. Phys. B: At., Mol. Opt. Phys. **34**, 4125 (2001).

[37] S. Fritzsche, A fresh computational approach to atomic structures, processes and cascades, Comput. Phys. Commun. **240**, 1 (2019).

[38] D. Coster and R. D. L. Kronig, New type of Auger effect and its influence on the x-ray spectrum, Physica **2**, 13 (1935).

[39] O. Jitrik and C. F. Bunge, Transition probabilities for hydrogen-like atoms, J. Phys. Chem. Ref. Data **33**, 1059 (2004).

[40] V. Bendkowsky, B. Butscher, J. Nipper, J. P. Shaffer, R. Löw, and T. Pfau, Observation of ultralong-range Rydberg molecules, Nature (London) **458**, 1005 (2009).

[41] J. Schwestka, D. Melinc, R. Heller, A. Niggas, L. Leonhartsberger, H. Winter, S. Facsko, F. Aumayr, and R. A. Wilhelm, A versatile ion beam spectrometer for studies of ion interaction with 2D materials, Rev. Sci. Instrum. **89**, 085101 (2018).

[42] S. Winecki, C. L. Cocke, D. Fry, and M. P. Stöckli, Neutralization and equilibration of highly charged argon ions at grazing incidence on a graphite surface, Phys. Rev. A **53**, 4228 (1996).

[43] N. Hatke, A. Hoffknecht, S. Hustedt, J. Limburg, I. Hughes, R. Hoekstra, W. Heiland, and R. Morgenstern, Energy loss of highly charged ions on an aluminum surface, Nucl. Instrum. Methods Phys. Res., Sect. B **115**, 165 (1996).

[44] H. Khemliche, J. Limburg, R. Hoekstra, R. Morgenstern, N. Hatke, E. Luderer, and W. Heiland, Energy loss and charge state distribution of reflected ions in N6,7+ ion-Al(110) surface collisions, Nucl. Instrum. Methods Phys. Res., Sect. B **125**, 116 (1997).

[45] E. Gruber, R. A. Wilhelm, R. Pétuya, V. Smejkal, R. Kozubek, A. Hierzenberger, B. C. Bayer, I. Aldazabal, A. K. Kazansky, F. Libisch *et al.*, Ultrafast electronic response of graphene to a strong and localized electric field, Nat. Commun. **7**, 13948 (2016).

[46] S. Creutzburg, A. Niggas, D. Weichselbaum, P. L. Grande, F. Aumayr, and R. A. Wilhelm, Angle-dependent charge exchange and energy loss of slow highly charged ions in freestanding graphene, Phys. Rev. A **104**, 042806 (2021).

[47] A. Niggas, S. Creutzburg, J. Schwestka, B. Wöckinger, T. Gupta, P. L. Grande, D. Eder, J. P. Marques, B. C. Bayer, F. Aumayr *et al.*, Peeling graphite layer by layer reveals the charge exchange dynamics of ions inside a solid, Commun. Phys. **4**, 180 (2021).

[48] V. Averbukh and L. S. Cederbaum, *Ab initio* calculation of interatomic decay rates by a combination of the Fano ansatz, Green's-function methods, and the Stieltjes imaging technique, J. Chem. Phys. **123**, 204107 (2005).

[49] A. Niggas, F. Aumayr, and R. A. Wilhelm, Trajectory-dependent highly charged ion-induced electron yield from single-layer graphene, Phys. Scr. **100**, 015403 (2025).

[50] W. S. M. Werner, V. Astašauskas, P. Ziegler, A. Bellissimo, G. Stefani, L. Linhart, and F. Libisch, Secondary electron emission by plasmon-induced symmetry breaking in highly oriented pyrolytic graphite, Phys. Rev. Lett. **125**, 196603 (2020).

[51] B. Baker, B. Johnson, and G. Maire, Photoelectric work function measurements on nickel crystals and films, Surf. Sci. **24**, 572 (1971).

[52] E. Galutschek, R. Trassl, E. Salzborn, F. Aumayr, and H. Winter, Compact 14.5 GHz all-permanent magnet ECRIS for experiments with slow multicharged ions, J. Phys.: Conf. Ser. **58**, 395 (2007).

[53] U. Kentsch, G. Zschornack, A. Schwan, and F. Ullmann, Short time ion pulse extraction from the Dresden electron beam ion trap, Rev. Sci. Instrum. **81**, 02A507 (2010).

[54] A. Gumberidze, M. Trassinelli, N. Adrouche, C. I. Szabo, P. Indelicato, F. Haranger, J.-M. Isac, E. Lamour, E.-O. Le Bigot, J. Mérot *et al.*, Electronic temperatures, densities, and plasma x-ray emission of a 14.5 GHz electron-cyclotron resonance ion source, Rev. Sci. Instrum. **81**, 033303 (2010).

[55] L. Skopinski, P. Ernst, M. Herder, R. Kozubek, L. Madauß, S. Sleziona, A. Maas, N. Königstein, H. Lebius, A. Wucher, and M. Schleberger, Time-of-flight mass spectrometry of particle emission during irradiation with slow, highly charged ions, Rev. Sci. Instrum. **92**, 023909 (2021).

[56] G. Greczynski and L. Hultman, A step-by-step guide to perform x-ray photoelectron spectroscopy, J. Appl. Phys. **132**, 011101 (2022).

[57] R. A. Wilhelm and P. L. Grande, Unraveling energy loss processes of low energy heavy ions in 2D materials, Commun. Phys. **2**, 89 (2019).

[58] L. Kalkhoff, A. Golombek, M. Schleberger, K. Sokolowski-Tinten, A. Wucher, and L. Breuer, Path to ion-based pump-probe experiments: Generation of 18 picosecond keV Ne+ ion pulses from a cooled supersonic gas beam, Phys. Rev. Res. **5**, 033106 (2023).